Experimental Investigation of Fracture–Matrix Flow Using CT Imaging

Ciprian-Teodor Panaitescu[1], *Kejian* Wu[1*], *Yukie* Tanino[1], *Andrew* Starkey[1], *Mehmet Emin* Kartal[1], and *Guan* Qin[2]

[1] School of Engineering, University of Aberdeen, Aberdeen, UK
[2]Cullen College of Engineering, University of Houston, Houston, Texas, USA

Abstract. Fracture–matrix fluid interaction is receiving growing attention in the energy sector, as it commonly occurs during hydraulic fracturing and injection operations designed to boost production or enable subsurface storage. This study examines how fluid flow evolves in sandstone reservoirs as fractures develop and interact with the surrounding matrix. Using a triaxial core flooding apparatus, we conducted experiments under coupled hydraulic and mechanical loading, capturing real-time pressure, flow, and stress data. Micro-CT imaging enabled direct visualisation of fracture initiation and propagation at the pore scale. The resulting dataset provides a basis to investigate the evolving fracture-matrix geometry and to quantify the interaction of fluid flow between fracture and matrix system, which will be used in the calibration of fracture-matrix pore network models. An important finding is that the fracture permeability is a function of matrix permeability in the Fracture–matrix coexisting system, there is an inverse correlation between the initial matrix permeability and the dimensionless fractured-to-unfractured permeability ratio (k_D), underscoring the control exerted by original rock properties. Despite overall permeability increases post-fracturing, flow remains intensely concentrated along fracture paths, with minimal contribution from the matrix. These results demonstrate the importance of experimental methods in quantifying fracture-matrix interactions, improving the understanding of fluid flow mechanism in fractured porous media during hydraulic fracturing and injection operations.

1 Introduction

Fluid flow in fractured geological formations plays a critical role in applications such as deep geothermal energy, hydrocarbon recovery, hydrogeology, and subsurface storage of hydrogen and carbon dioxide [1,2]. The interaction between fracture and matrix flow is gaining increasing attention in the energy industry due to its prevalence in hydraulic fracturing and injection processes aimed at enhancing production or subsurface storage [3,4]. Understanding flow behaviour in these systems is essential across various industrial sectors. While this study focuses on single-phase incompressible flow, the interaction between matrix and fracture domains during the fracturing process presents a complex and valuable area for experimental investigation.

Although fractures typically represent a minor contribution to total rock porosity, their significantly higher permeability allows them to dominate overall fluid transport [5]. The interaction between fracture networks and the surrounding rock matrix is crucial in controlling fluid migration [6,7]. However, these interactions remain poorly understood, especially under dynamic conditions involving fracture propagation.

Conventional modelling approaches, such as dual-porosity and dual-permeability frameworks, provide useful conceptualisations of fracture-matrix systems but often oversimplify the physics by assuming static geometries, uniform fracture distributions, and limited matrix-fracture exchange [8,9]. These limitations become especially pronounced during active fracture propagation, where fluid flow grows increasingly complex and spatially heterogeneous due to evolving fracture geometries and stress-dependent permeability.

To address this gap, high-resolution, in situ experimental observations are necessary. This study presents an integrated experimental framework designed to quantify fracture-matrix interactions during fracture progression in sandstone core samples under realistic subsurface conditions. The experiments utilise a coupled triaxial geomechanical-hydraulic setup that simultaneously measures stress, flow rate, and pressure gradients. This is combined with time-lapsed, multi-resolution micro-CT imaging to directly capture fracture initiation, growth, and connectivity in three dimensions, as well as the evolution of pore structure during loading.

Both single-layer and multilayer reservoir rock samples are tested to examine the role of geological heterogeneity and anisotropy in controlling fracture development and fluid flow behaviour. Layered composites provide valuable insights into fracture propagation across contrasting mechanical and hydraulic units, replicating field-relevant conditions. From these experiments, a rich dataset is obtained, including mechanical response, flow measurements, and high-resolution 3D images of evolving fracture and pore structures.

The experimental results are the foundation for constructing and calibrating digital rock models incorporating realistic fracture and matrix geometries. While the full modelling framework will be detailed in a companion study, the present work focuses on the experimental observations and flow behaviour, offering new insights into how fracture propagation governs flow partitioning between fractures and the matrix. In particular, we observe the onset of preferential flow pathways along newly formed fractures, with matrix contribution varying depending on pore connectivity and stress conditions.

---

* Corresponding author: kejian.wu@abdn.ac.uk

By advancing experimental techniques that explicitly resolve fracture-matrix interactions in situ, this work provides a critical step forward in understanding the mechanics of fluid transport in fractured rocks. The findings have broad implications for optimising resource extraction and storage strategies in heterogeneous reservoirs and for improving the predictive capabilities of coupled flow-geomechanics models.

2 Materials and methods

This section describes the experimental framework for studying fracture–matrix fluid interactions in sandstone under controlled stress and flow conditions. Core samples sourced from a North Sea reservoir were prepared according to the requirements of the experimental setup, as outlined in the following subsection. A portable, custom-built triaxial flow apparatus was developed to accommodate both the hydraulic testing and high-resolution imaging workflow. The methodology comprises three parts: sample description and preparation, apparatus design, laboratory testing procedure, and a digital analysis workflow that focuses on the deep learning segmentation algorithm implemented.

2.1 Sample selection and preparation

2.1.1 Sample information

A subset of 15 sandstone core plugs was chosen from a larger set of 160 two-inch diameter cores to experimentally investigate the interaction between fracture and matrix flow in sandstone. These cores were drilled from sandstone reservoir formations in the Southern and Central North Sea fields. Five of the 15 selected cores were used to fabricate three composite plugs, following the preparation procedure outlined in this section.

Sample selection was based on a range of porosity and permeability values to ensure that the final subset represented combinations of high and low extremes in each property. The porosity values among the selected cores ranged from 4.8% to 22%, while permeability varied from 0.13 to 300 mD. Properties for two representative samples are summarised in Table 1.

Table 1. Sample properties: porosity (ϕ) and permeability (k).

Sample	ϕ [%]	k [md]
Composite sample	15.4	105.14
Single-matrix sample	13.3	15.4

2.1.2 Sample preparation

The original core plugs measured 50.8 mm in length, but a length-to-diameter ratio of at least 2:1 is recommended for reliable laboratory testing [10]. Additionally, for the composite samples, where heterogeneity plays a central role, it was essential to ensure that each segment was sufficiently large to represent its respective formation. A reduction in core diameter to 25.4 mm was found to satisfy both the geometric constraint and the requirement for heterogeneity representation. All selected samples were resized to this diameter using a pillar drill fitted with a diamond coring bit.

For composite sample preparation, two core plugs with contrasting permeability properties were cut longitudinally using a benchtop saw equipped with a diamond blade. The resulting segments were then dried for 24 hours before assembly. Each pair was carefully aligned and bonded with an epoxy adhesive, then cured for another 24 hours. To ensure stability during handling and machining, the assembled plug was wrapped in shrink film and cored to a final diameter of 25.4 mm, matching the single-matrix plugs.

The resulting composite (or dual formation material) structure had a cross-sectional configuration consisting of two-thirds low-permeability sandstone and one-third high-permeability sandstone. The low-permeability region was targeted for induced fracturing during the experiments, mimicking the typical fracturing strategy used in field applications. Meanwhile, the higher-permeability material occupied the remaining one-third of the plug. It is worth noting that the high-permeability sandstone, sourced from the North Sea reservoir, was friable, which limited the number of usable segments that could be extracted from each parent core.

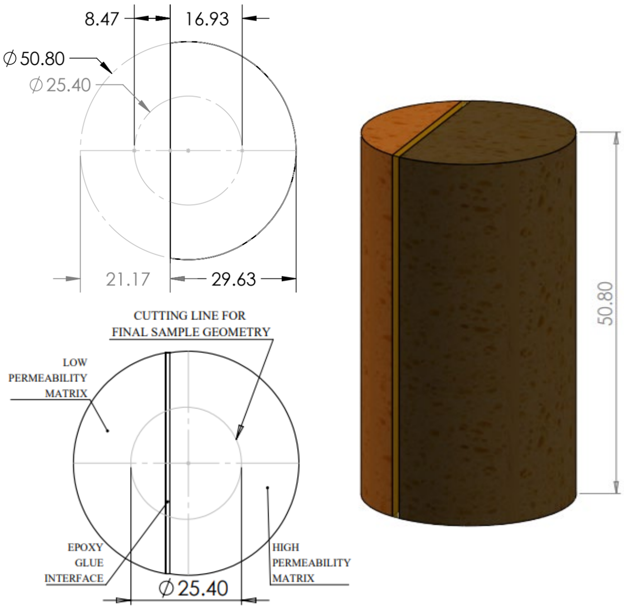

Fig. 1. Sample preparation illustrating (left) the cutting line schematic from a single matrix, (middle) the composite sample combination schematic, and (right) the cutting result of the two samples.

2.2 Apparatus description

To accommodate this study's coupled imaging and mechanical loading requirements, a modified triaxial flow apparatus was developed, extending a previous design [11], shown in Figure 2. The revised setup integrates continuous flooding ports and support structures optimised for micro-CT compatibility. A key addition is the inclusion of 3 mm-thick, machined semicircular aluminium spacer inserts, adapted from [12], which direct fracture propagation by modifying localised shear stress.

The apparatus consists of a precision-machined aluminium cylinder (31 mm ID and 50 mm OD) fitted with a nitrile sleeve that isolates the sample and confines the fluid domain. Perforated flow pathways are incorporated above and below the sample for fluid input and air venting. Confining pressure is applied through hydraulic fluid via the lower port, with pressure retained by interlocking collars and tapered seals.

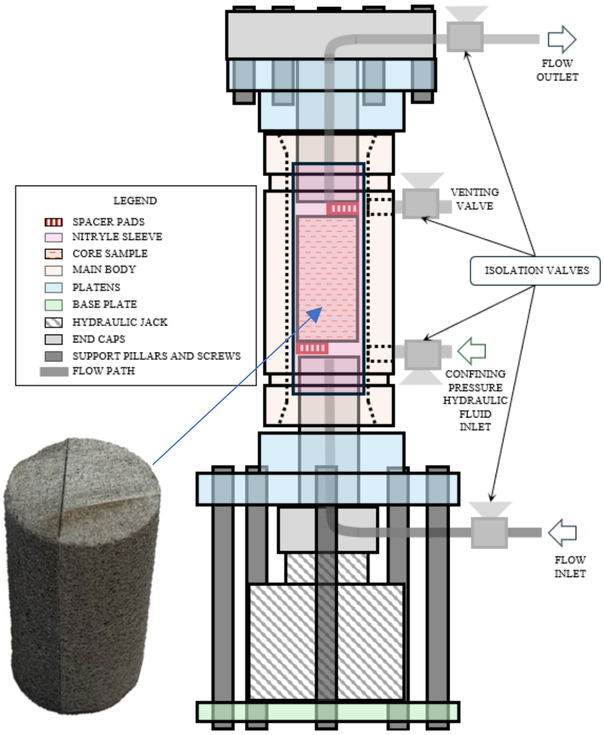

Fig. 2. Schematic of the triaxial-flow cell.

The sample is axially loaded using a hydraulic jack interfaced with a mobile lower platen, which travels within the cell as deformation occurs. The fixed upper platen, secured with six screws, maintains alignment. Both platens are internally perforated (3.175 mm diameter) to allow fluid flow during flooding tests, with connections routed to a Teledyne ISCO 1000D syringe pump. The system design minimises obstruction of the scanning field, enabling in situ observation under load.

Pressure data are collected through four sensors (APB3-0400 and UNIK 5000), linked to a National Instruments data acquisition unit and monitored in real time via LabView. Figure 3 shows the experimental setup for the flow and mechanical fracturing tests.

Fig. 3. Image of the fracturing and flow measurement experimental apparatus.

The spacer pads are essential in guiding fracture development, as their positioning depends on the sample type. For mono-facies plugs, they induce vertical fractures aligned orthogonally to the imaging plane. The composite cores are aligned along the bonded interface, parallel to the 0.25 mm epoxy interface, and secured against lateral shifting with a fine textile mesh to promote propagation exclusively through the lower-permeability section. A fine mesh ensures consistent placement before loading.

3 Image segmentation methodology

3.1 Imaging and Image Processing

Micro-CT imaging was carried out using a ZEISS VersaXRM-410 microscope, optimised for multi-resolution scanning of cylindrical rock samples [13]. The cell placement inside the micro-CT scanner is shown in Figure 4. The scanner was configured with an X-ray beam energy of 140 kV and a power output of 10 W, using a 0.4× optical magnification to match the field-of-view to the sample geometry.

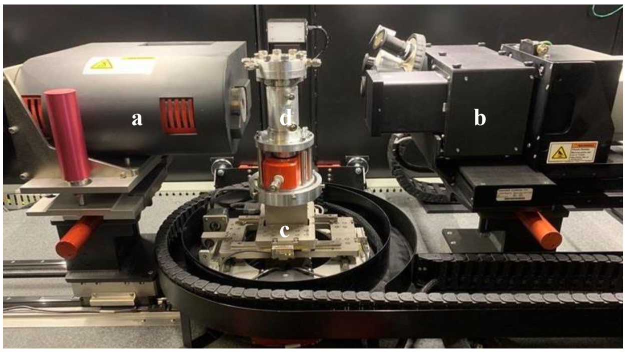

Fig. 4. Labelled picture of the in-situ micro-CT scanning setup. (a) X-ray source, (b) X-ray receiver, (c) rotating stage and (d) compact triaxial-flow cell with isolation valves closed to ensure the in-situ condition is retained.

Two scan modes were employed: high-resolution for pore-scale analysis and low-resolution for fracture mapping. The high-resolution scans (binning of 1) produced projections at 2048 × 2048 pixels, while the low-resolution scans (binning of 2) reduced this to 1024 × 1024 pixels. These settings corresponded to pixel sizes of approximately 12.7 µm and 25.4 µm, respectively. To improve signal-to-noise ratios, radiographic exposure durations were set to 4.5 seconds for high-resolution and 7.5 seconds for jacketed low-resolution scans. Each scan collected 2700 projections over a 360° rotation. Reconstructed images were produced using Xradia XMReconstructor, with corrected beam hardening and center-shift artifacts [14].

This dual resolution approach was necessary due to the inherent trade-off between spatial resolution and field of view, a constraint common to micro-CT systems. Higher resolution enables detailed pore analysis but restricts volumetric coverage, while lower resolution allows for fracture-scale observations within the entire sample. Thus, a two-stage workflow was used: detailed pore segmentation from unjacketed scans and full-core fracture analysis from jacketed scans. Cross-sectional slices from the resulting scanned volumes using both the high and low resolution settings are shown in Figure 5.

The digital image processing pipeline consisted of:

（1）Slice alignment and stacking correction to remove spatial jitter during acquisition, as well as any tilting caused by the fracturing process

（2）Noise filtering to enhance feature visibility, especially the void (both pore and fracture) and solid interface

（3）Pore-grain segmentation for the high-resolution scan and pore-fracture-grain segmentation for the low-resolution scan

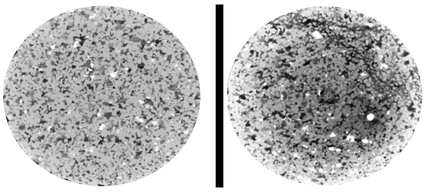

Fig. 5. Slices from micro-CT imaging of the single-matrix sample. The left row shows the high-resolution scan of the unfractured sample, while the right presents the lower-resolution in-situ scan acquired after fracturing.

Initial segmentation classified solid versus void regions using intensity-based thresholding. However, due to similar grayscale values, this approach alone was insufficient to separate overlapping features like large pores and microfractures. Attempts using traditional techniques such as Otsu's method and multi-threshold approaches yielded inconsistent results. As a result, a convolutional neural network (CNN) approach was introduced to achieve pixel-wise classification of matrix, pores, and fractures. This AI-based method is further elaborated in the following section.

3.2. Deep learning segmentation

To address the insufficient segmentation and poor capacity to delineate between pores and fractures of traditional segmentation, a convolutional neural network (CNN) approach inspired by the U-Net architecture [15] was implemented. This methodology has proven effective in similar geological image analyses such as [16-19].

A schematic overview of the full segmentation pipeline is shown in Figure 6. The workflow begins by importing micro-CT grayscale scans of unfractured rock, experimental porosity data, and a library of segmented fracture geometries compiled from literature, including [20-23]. Adaptive thresholding was successful in segmenting high-resolution un-fractured rock images, so this was used as a step in creating the training dataset, as it is applied to generate solid/void masks, which are iteratively refined based on their match with experimental porosity measurements.

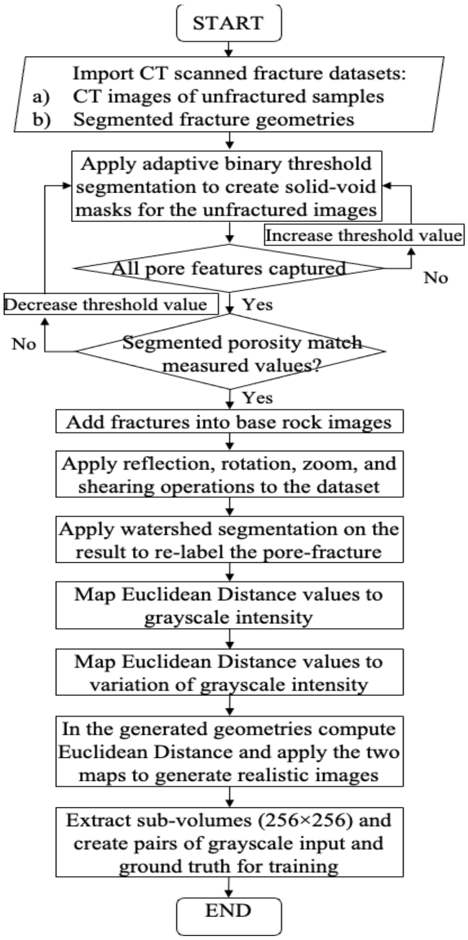

Fig. 6. Workflow for generating synthetic fractured rock volumes for deep learning training.

Synthetic fractures are embedded into these segmented volumes to generate two geometries: (1) cleanly intersecting fractures and (2) fractures that induce morphological deformation in intersected grains, simulating shear behaviour. Controlled data augmentation techniques (rotation, zoom, noise injection, etc.) are applied to expand the dataset, which is especially important given the limited availability of real fractured samples.

The segmentation accuracy is further enhanced by incorporating contextual grayscale information derived from the Euclidean Distance Transform (EDT [24]). Two auxiliary neural networks are trained to map EDT to expected grayscale intensity and its local variability, enabling the generation of more realistic training images in grayscale space. The overall workflow for producing the training dataset is shown in Figure 6.

The final CNN model is trained using weights pre-initialised on ImageNet-21k [25], with a hybrid loss function that combines Focal Loss [26,27] and Minkowski Loss [27], thereby addressing both class imbalance and preserving geometrical-topological consistency. This setup achieved Jaccard similarity scores of 0.86 for 2D segmentation. The CNN architecture used is depicted in Figure 7.

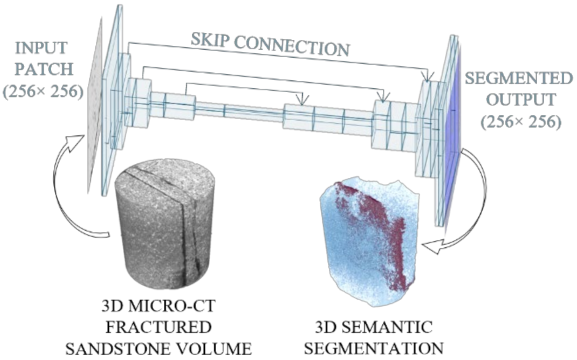

Fig. 7. Convolutional Neural Network architecture following the U-Net convention. The encoder path consists of sequential 3D convolutions with ReLU activations, followed by max pooling layers. The decoder path includes up-convolutions and feature concatenation with corresponding encoder layers via skip connections. The network input is a micro-CT volume, where fractures are shown in red, pores in blue, and solid grains are rendered transparent.

4 Experimental measurement and flow quantification analysis

4.1 Triaxial fracturing experiments

The triaxial dynamic fracturing experiments were conducted under a starting confining pressure of 250 psi, which was kept constant unless the internal inlet pressure reached a value of 200 psi, after which point the confining pressure was continuously adjusted to maintain the 50 psi difference, which would ensure sealing. This difference has been determined as sufficiently large by running a series of experiments at different confining and inlet pressures, investigating the difference necessary to prevent bypass flow.

Due to the rig material constraints, very large axial loads were avoided. The confining pressure must be minimised while maintaining the seal to ensure these loads are not necessary for fracturing. The solution we proposed to achieve this low differential is the lateral coating of the core sample with a uniform layer of ductile wax, which improves the contact between the rough rock surface and the rubber sleeve that isolates the interior flow domain from the hydraulic oil used to transfer the confining pressure. In addition to helping to lower the necessary axial load, the low confining pressure also assists in producing fractures with a low inclination angle, resulting in an improved inlet-to-outlet connection and aiding in controlling the propagation exclusively in the desired matrix segment in the case of the composite experiment.

The flow rate was also designed to allow for the low confining pressure whilst maintaining a flow sufficiently large to measure changes due to the evolving fracture. As the fracture develops, the pressure gradient necessary to sustain a constant flow rate drops significantly. Selecting a sufficiently large starting flow rate must account for this fact. To ensure this, the pre-tests included testing the sample with flow rates between 1 and 10 mL/min to choose the most appropriate constant flow rate pump setting.

Throughout the experiment, the flow regimes remained within the Darcy flow regime, with Reynolds numbers not exceeding 0.004 based on the original flow rate, and the mean pore diameter was considered the characteristic length. This was true even after fracturing, where the fracture aperture was included in the computation of the characteristic length. As fracturing initiated and progressed, the permeability increased, gradually reducing the cross-sample pressure difference necessary to maintain a constant flow rate due to the opening of the fracture.

Multi-scale scanning is a critical part of the study, providing information on the matrix pore characteristics and the fracture parameters. We conducted un-jacketed high-resolution scans of the dry samples before using them for the triaxial-flow test. After the test was concluded, in-situ scans were taken to characterise the fractures without allowing for their further displacement, albeit at lower resolution.

4.2 Dynamic Flow Test Conditions and Flow Regimes

After the sandstone core sample has been fully saturated, the dynamic hydraulic flow testing coupled with triaxial geomechanics was conducted under injecting water at a constant inlet pressure of 200 psi, selected with a confining pressure of 250 psi. This pressure differential ensured complete sample sealing within the nitrile sleeve, preventing any bypass flow throughout the experiment. The confining pressure remained significantly higher than the inlet pressure at all points along the flow path, particularly at the sample inlet, where the pressure was maximal due to the nature of porous media flow.

Although the inlet pressure was nominally fixed at 200 psi, the pump occasionally stabilised at a slightly lower pressure. This occurred when the system could not sustain the set point under evolving permeability conditions, particularly toward the end of the test. Despite this, flow field stabilisation was verified at both the beginning and end of each experiment to ensure reliable interpretation of results.

The test followed a constant flow rate protocol for the composite sample, with the pump set to deliver 5 mL/min throughout the experiment. The recorded flow rate evolution revealed transitions across multiple flow regimes as the sample underwent deformation. A reduced porosity along the vertical axis initially caused a temporary pressure dip. This was followed by a rapid increase in flow rate corresponding to the onset and progression of fracture propagation. Eventually, the system entered a linear flow regime indicative of stable fracture flow.

The fractured-to-unfractured permeability ratio was selected as the key metric to quantify the impact of fracturing on flow behaviour. This dimensionless ratio reflects the permeability enhancement resulting from the presence of the fracture.

Notably, the maximum fractured-to-matrix permeability ratio observed during testing was approximately 5.5, subsequently stabilised by the experiment’s conclusion. This trend underscores the significant enhancement in fluid transmissivity introduced by the induced fracture network.

5 Results and discussion

This section presents the experimental findings alongside observations from micro-CT imaging. It begins with an overview of the pore network characteristics of the un-fractured core plugs, as determined by high-resolution scans. A central metric in the analysis is the dimensionless ratio of post- to pre-fracturing permeability, introduced to quantify the impact of fracture development. The discussion then shifts to a detailed examination of flow dynamics, particularly emphasising the changes observed during fracture initiation and propagation.

5.1 Un-fractured sample characterisation

Table 1 presents the porosity and permeability measurements for the single-matrix sample and the individual components of the composite sample. High-resolution micro-CT scanning enabled the extraction of pore-scale geometric features, facilitating the quantification of key pore network statistics. The hydraulic pore radius, calculated based on both volume and surface area, ranged from 19 µm to 150 µm, with some minimum values falling below the scan resolution due to the irregularity of pore shapes.

The mean hydraulic pore radius for the single-matrix sample was 59.0 µm, with a standard deviation of 29.5 µm and a positive skewness of 0.9. Throat sizes had a mean of 36.4 µm, a standard deviation (SD) of 15.0 µm, and a skewness of 0.85. The average pore shape factor was 0.0381, and for throats, it was 0.0370, with standard deviations of 0.0106 and 0.0112, respectively. These distributions were well approximated by standard probability functions. The mean pore coordination number was 3.29.

In the composite sample, the lower-volume (low-permeability) segment showed a mean pore radius of 53.99 µm (SD: 13.92 µm, skewness: 0.25) and throat radius of 37.73 µm (SD: 9.13 µm, skewness: 0.42). The corresponding shape factors were normally distributed, with means of 0.0424 (SD: 0.0071) for pores and 0.0431 (SD: 0.0086) for throats.

The higher-permeability segment used in the composite had a mean pore radius of 69.32 µm (SD: 21.22 µm, skewness: 0.20) and a mean throat radius of 49.14 µm (SD: 14.29 µm, skewness: 0.48). In this case, the pore and throat shape factors were 0.0398 (SD: 0.008) and 0.0396 (SD: 0.009), respectively.

The average coordination numbers for the low- and high-permeability segments were 2.90 and 3.12. These metrics serve as a baseline for comparison with the composite samples analysed later in the study.

5.2 Flow Evolution under Share Fracturing in the core Sample

The experimental procedure for the single-matrix sample has been conducted under constant pressure conditions (with the pump inlet providing a steady inlet pressure of 200 psi). This value was selected in conjunction with the confining pressure value of 250 psi, which must be maintained permanently and significantly above pressures at any point in the sample to ensure no bypass flow. Due to the essential physics of porous media flow, this maximum value is at the sample inlet; hence, this setting provides the sealing of the rubber sleeve.

Additionally, as observed at the end of the test, despite the intended constant pressure setting, the pump may be unable to supply the required pressure, stabilising at a constant, albeit lower, sustainable pressure under this specific final permeability of the sample. Flow field stabilisation has been sought and ensured both at the beginning and end of the test. The increase in flow rate also highlights multiple flow regimes during the sandstone failure period (including a rapid decrease in pressure due to porosity reduction along the vertical axes, followed by a fast flow rate increase and a linear increase regime, which can be explained by the fracture propagation regime).

The ratio of the current instantaneous permeability (k_F) to the original permeability of the sample (k_U), defined in Equation 1, is an important dimensionless parameter summarising these flow field changes.

$$k_D = \frac{k_F}{k_U} \tag{1}$$

Connecting fracture systems increase permeability, causing the dimensionless ratio to exceed one. In contrast, fracture closing, plugging, and matrix compaction may be possible in unconsolidated sandstone samples, which may drive k_D to a sub-unitary value.

Once the flow field stabilises, both the denominator and the numerator are correctly defined as permeability values representing steady-state measurements [28]. However, applying this definition to the dynamic process allows us to analyse the dynamic changes in fluid, simultaneously capturing both pressure and flow rate variations.

The flow rate, pressure, and k_D are shown for the single and composite samples in Figures 8 and 9, respectively. Additionally, the maximum fracture-to-matrix permeability ratio achieved was 5.5, produced after the test was applied to the single-matrix sample, representing the ratio of well-defined permeability as the flow field stabilised.

The experiment was conducted at a constant applied flow rate for the single-matrix sample, though significant changes in permeability during fracture growth necessitated adjustments in the pressure differential. As permeability increased, the system could not maintain the original pressure setting, and the pressure gradually stabilised at a lower level, as illustrated in Figure 8.

Despite this reduction, flow field stability was confirmed both at the beginning and end of the test, ensuring that the permeability measurements remained reliable. Using the dimensionless fractured-to-unfractured permeability ratio (k_D) provides a clear metric for assessing the combined mechanical and flow evolution. Figure 8 presents the plots of inlet pressure, flow rate, axial load, and the instantaneous permeability ratio.

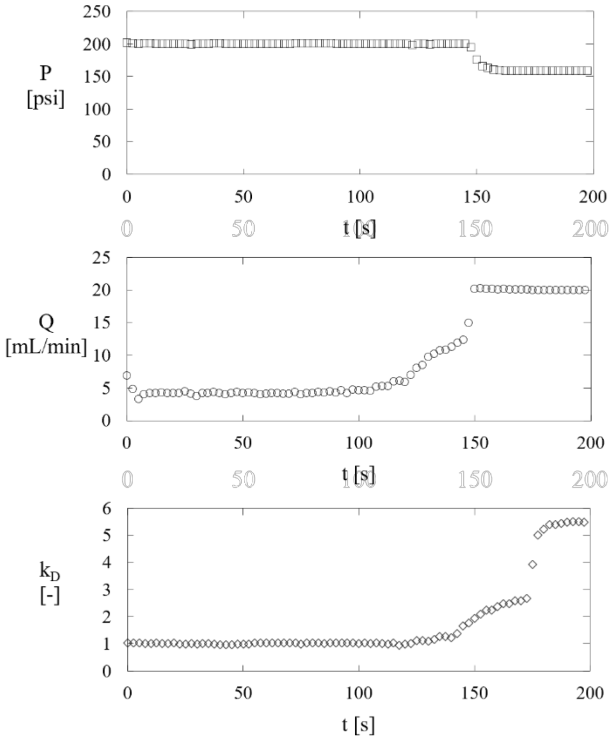

Fig. 8. Evolution of the flow behaviour for the single-matrix sample: pressure (P), flow rate (Q), fractured-unfractured permeability ratio (kD) over time (t).

As shown in Figs. 8 and 9, fracture initiation is marked by an increase in flow velocity and a corresponding rise in core permeability. The continued increase in permeability indicates progressive fracture propagation, eventually leading to full breakthrough, which is accompanied by a drop in vertical loading pressure. Flow behaviour during the test revealed distinct stages associated with fracture development. An initial pressure drop marked the onset of fracture initiation, followed by a gradual increase in flow velocity as the fracture advanced. Once the fracture was fully connected to the top and bottom boundaries of the sample, the flow rates sharply increased. The supply pressure became insufficient at this stage for the now high-permeability system. This led to a further decline in pressure before a new steady state was established, as reflected in the normalised permeability trend.

In the composite sample case, shown in Figure 9, the maximum k_D achieved reached a lower value of 3.5. This is attributed to the initial contribution of the high-permeability layer within the composite sample, which provided a dominant flow path even before significant fracturing of the low-permeability matrix occurred. Once fracture development was initiated in the low permeability rock, fluid redistribution occurred between the induced fracture and the pre-existing high-permeability material. Similar flow stages were observed, although the competition between the two effective flow pathways introduced additional complexity in flow behaviour.

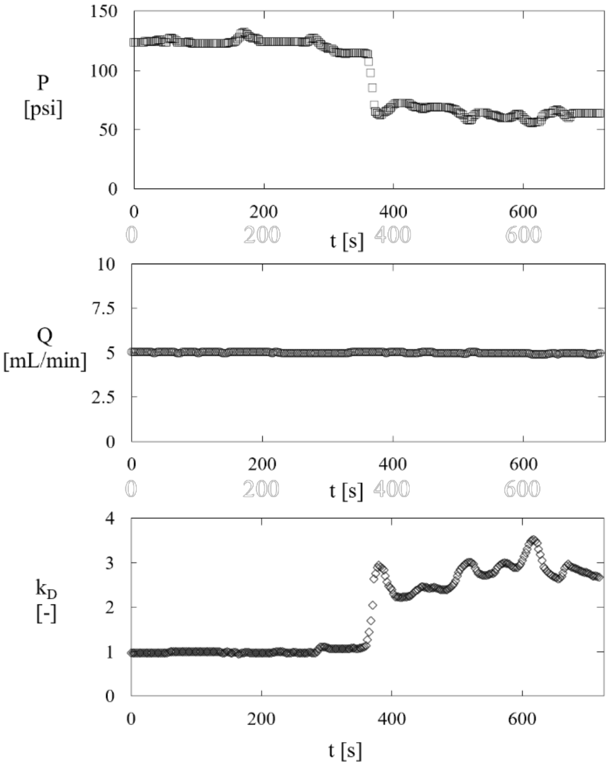

Fig. 9. Evolution of the flow behaviour for the composite sample: pressure (*P*), flow rate (*Q*), fractured-unfractured permeability ratio (k_D) against time (*t*).

To fully understand the fracture-matrix system, computational modelling provides valuable support in characterising the evolving flow fields. During dynamic fracturing with water injection, fluids preferentially migrate through larger fracture apertures, called seepage capture or laminar flow partitioning. The degree of this flow redirection significantly depends on the matrix pore size distribution.

Analysis indicates that the fractured-to-unfractured permeability ratio is inversely related to the original matrix permeability: lower matrix permeabilities show greater sensitivity to fracture-induced flow enhancement, as illustrated in Figure 10.

The relationship presented between the fractured flow behaviour and the matrix properties is due to the significantly larger size contrast between fracture voids and matrix pores in tight formations, amplifying the dominance of fractures in fluid transport.

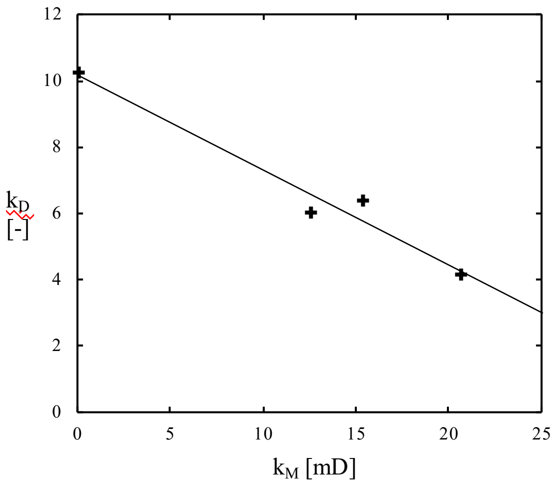

Fig. 10. Fractured permeability over unfractured permeability ratio (k_D) as a function of initial matrix permeability (k_M), showing the inversely proportional correlation in single-matrix samples.

6 Conclusions

This work presents a comprehensive experimental investigation into the evolution of flow behaviour during fracture propagation in sandstone under coupled mechanical and hydraulic conditions. Using a custom triaxial flow cell and in situ micro-CT imaging, we observed the progressive development of fractures and their effect on permeability and flow distribution in both single-layer and composite sandstone samples.

The results show that water injection under controlled stress conditions leads to significant permeability enhancement, with increases ranging from 2.5× to 10× relative to initial values. This is attributed to the preferential channelling of fluid through newly formed fractures, effectively diverting flow away from the matrix. The extent of this flow partitioning was influenced by matrix properties, particularly pore size distribution and initial permeability, reinforcing the importance of matrix-fracture interaction in heterogeneous formations.

In composite samples, fracture propagation was effectively directed into the low-permeability segment through controlled sample design. Flow measurements and imaging confirmed that the matrix still contributed to total permeability, although its relative influence diminished as fractures evolved. Quantitative image analysis revealed that fracture apertures ranged from 10 to 400 µm and were associated with localised porosity increases between 1–3%.

CNN-based segmentation and digital modelling approaches were successfully used to support interpretation, achieving excellent accuracy of 0.86 based on the Jaccard metric, and demonstrating the importance of the machine learning segmentation step as an essential tool for the present analysis.

Overall, this study examines how fluid flow evolves in sandstone reservoirs as fractures develop and interact with the surrounding matrix. The results presented here contribute to a deeper understanding of fracture-matrix interactions and highlight key mechanisms controlling fluid redistribution during fracturing. These insights are relevant to a wide range of subsurface applications, including enhanced oil recovery, geothermal production, and underground energy storage. The results of this study give a solid quantification of fracture–matrix fluid interaction that is growing attention in the energy sector, as it commonly occurs during hydraulic fracturing and injection operations designed to boost production or enable subsurface storage.

References

1. B. Berkowitz, Adv. Water Resour. **25**, 861 (2002).
2. D. Crandall, G. Ahmadi, D.H. Smith, Transp. Porous Media **84**, 493 (2010).
3. Warpinski, N. R., & Teufel, L. W. (1994). Journal of Petroleum Technology, **46**(02), 209–215.
4. Zoback, M. D. (2007). Reservoir Geomechanics. Cambridge University Press.
5. J.P. Aguilar-López, T. Bogaard, H.H. Gerke, Water Resour. Res. **56**, (2020).
6. Wen, B., Benson, P. M., & Meredith, P. G. (2019). Journal of Geophysical Research: Solid Earth, **124**(1), 346–364.
7. Fisher, K., & Warpinski, N. (2012). SPE Production & Operations, **27**(01), 8–19.
8. K.B. Nakshatrala, S.H.S. Joodat, R. Ballarini, J. Appl. Mech. **85**, (2018).
9. E. Tuncay, N. Hasancebi, Bull. Eng. Geol. Environ. **68**, 491 (2009).
10. A. Syed, Y. Tanino, J.M. Lamanna, D.L. Jacobson, D.S. Hussey, E. Baltic, G. Burca, Meas. Sci. Technol. **32**, 095403 (2021).
11. L.P. Frash, J.W. Carey, Z. Lei, E. Rougier, T. Ickes, H.S. Viswanathan, J. Geophys. Res. Solid Earth **121**, 5493 (2016).
12. M.E. Kartal, L.H. Dugdale, J.J. Harrigan, M.A. Siddiq, D. Pokrajac, D.M. Mulvihill, J. Mater. Sci. **52**, 10186 (2017).
13. J.C. Hastie, M.E. Kartal, L.N. Carter, M.M. Attallah, D.M. Mulvihill, Mater. Charact. **163**, (2020).
14. O. Ronneberger, P. Fischer, T. Brox, *Lecture Notes in Computer Science (Including Subseries Lecture Notes in Artificial Intelligence and Lecture Notes in Bioinformatics)* **9351**, 234 (2015).
15. C.T. Panaitescu, K. Wu, Y. Tanino, A. Starkey, Granite **8**, (2023).
16. B. Wang, Y. Feng, J. Du, Y. Wang, S. Wang, R. Yang, SPE J. **23**, 567 (2018).
17. S. Karimpouli, P. Tahmasebi, E.H. Saenger, Nat. Resour. Res, **29**, 1675 (2020).
18. J. Kim, G.J. Moridis, SPE J. **19**, 1110 (2014).
19. Z.T. Karpyn, A.S. Grader, P.M. Halleck, J. Colloid Interface Sci. **307**, 181 (2007).
20. Z.T. Karpyn, A. Alajmi, F. Radaelli, P.M. Halleck, A.S. Grader, Eng. Geol. **103**, 139 (2009).

21. M.J. Ramos, D.N. Espinoza, C. Torres-Verdín, T. Grover, Geophysics **82**, (2017).
22. K. Sawayama, T. Ishibashi, F. Jiang, T. Tsuji, Y. Fujimitsu, Rock Mech. Rock Eng. **54**, 2145 (2021).
23. Mishchenko, Signal Image Video Process **9**, 19 (2015)
24. Ridnik, E. Ben-Baruch, A. Noy, L. Zelnik-Manor, *ImageNet-21K Pretraining for the Masses* (2021).
25. M. Yeung, E. Sala, C. B. Schönlieb, L. Rundo, Comput. Med. Imaging Graph. **95**, (2022)
26. P. Yun, L. Tai, Y. Wang, C. Liu, M. Liu, IEEE Robot. Autom. Lett. **4**, 1263 (2019).
27. C.T. Panaitescu, K. Wu, M.E. Kartal, Y. Tanino, A. Starkey, G. Qin, L. Zhao, Z. Cao, S. Wu, *SPE Europe Energy Conference and Exhibition, EURO 2024* (SPE, Turin, 2024).
28. J. Bear, Y. Bachmat, *Introduction to Modelling of Transport Phenomena in Porous Media* (Kluwer; Theory and Applications of Transport in Porous Media, **4**, 1990).